

# Chapter 7

## Foreshore Applications of X-band Radar

G.M. Jahid Hasan and Satoshi Takewaka

**Abstract** The shallow waters of a nearshore region are dynamic and often hostile. Prediction in this region is usually difficult probably by our limited understanding of the physics or by availability of accurate field data. It is a challenge for traditional in situ instruments to provide these inputs with the appropriate temporal or spatial density at a reasonable cost. Remote sensing provides an attractive alternative. An X-band nautical radar system was employed for this study to examine alongshore propagation of low frequency run-up motion around the research pier HORS in Hasaki beach, Japan. Analyses on radar echo images were done to estimate longshore distribution of shoreline positions and inter-tidal foreshore profile using time-averaged images. Spatio-temporal variation of water fronts were digitized manually from cross-shore time-stack images. Run-up heights were then estimated from the digitized water fronts with the help of foreshore slope. Run-up variations under dissipative condition were parameterized with surf similarity parameter. Low frequency variances in the run-up motion were observed, which were traveling in the longshore direction. Longshore structures of this motion were examined and compared with different wave incidences during two typhoon events in the Pacific Ocean. Estimates of morpho-dynamic parameters during passage of different storms were analyzed and are explained in this chapter to demonstrate the potential of radar measurement in capturing essential characteristics of foreshore dynamics.

---

G.M.J. Hasan (✉)

Department of Civil and Environmental Engineering, Shahjalal University of Science and Technology, Sylhet 3114, Bangladesh

Department of Civil Engineering, Military Institute of Science and Technology, Dhaka 1216, Bangladesh

e-mail: [jahid01@yahoo.com](mailto:jahid01@yahoo.com)

S. Takewaka

Department of Engineering Mechanics and Energy, Graduate School of Systems and Information Engineering, University of Tsukuba, Tsukuba, Ibaraki 305-8573, Japan

e-mail: [takewaka@kz.tsukuba.ac.jp](mailto:takewaka@kz.tsukuba.ac.jp)

## 7.1 Introduction

The nearshore is the narrow strip of the ocean that borders the continents. It can be dynamically defined as the coastal region that is significantly affected by gravity waves, and spans from inland reach to an offshore depth of  $O(10\text{ m})$  beyond which bathymetric change is no longer due to wave motions. The nearshore is the energetic region of the coastal environment where ocean waves shoal and interact with local morphology. The nearshore is a difficult domain to sample and understand. As waves approach an open shoreline from deep water, they undergo several changes. Breaking waves in the surf zone are often intense and wave-driven currents can be strong, which makes work in the surf zone dangerous to both people as well as instruments. Changes in bathymetry can occur on time scales as short as hours due to presence of large storms. Sandy beds can undergo substantial erosion or accretion within short periods, so traditional bottom-mounted sensors are often rapidly scoured out or buried in.

Data are especially difficult to collect in nearshore region during periods of large waves or strong currents. However, these conditions often represent the most energetic periods for hydrodynamics, morpho-dynamics and are the times of greatest scientific interest. The harsh and challenging conditions make long-duration in situ observations in the surf zone problematic but suggest the potential benefits of remote sensing approaches. Although most people associate remote sensing with satellites, a number of other solutions are available, from airborne sensors on manned and unmanned platforms to shore-based sensors mounted on lighthouses, towers or bluffs. All have the advantage that sensors can be installed away from harsh marine conditions; can often have direct access to the power grid, storage, and the internet; and can usually observe a large spatial extent over long durations at a low cost.

The nearshore can be sampled by a full suite of both active and passive remote sensors (cameras, radars, lidars, etc.) using a range of platforms (fixed, flying, floating, and orbiting) and operating across the visible, infrared (IR), microwave, and radio bands of the electromagnetic (EM) spectrum in addition to the in situ sensors. However, for nearshore oceanographic applications, fixed optical cameras and X-band radars are used the most frequently nowadays.

### *7.1.1 Requirements of Nearshore Monitoring System*

The dynamics of the nearshore are driven primarily by ocean wave energy that has been generated elsewhere and propagated into the nearshore domain. Unlike the deeper ocean, the dissipation of nearshore energy occurs in a narrow strip due to depth limitation. These processes generally drive nearshore currents and circulation as well as the sediment transport that creates nearshore sand bars and complex bottom morphology.

The goal of nearshore science is to understand, characterize, and predict the evolving waves, currents, and bathymetry over any nearshore region for which

observations are available. Solutions have inevitably consisted of numerical models, which have shown increasing skill when fed with accurate bathymetry and wave data (e.g., Ruessink et al. 2001). For all but a few well-instrumented field sites, prediction accuracy is limited by data availability, particularly for bathymetry data, gathering of which usually requires expensive sampling methods and can be done only occasionally. Thus, data assimilation methods must be used to merge available observations with models to yield dynamically consistent estimates of flow variables and bathymetries (e.g., Wilson et al. 2010).

The requirements for successful sampling of the nearshore are governed by the time and space scales of variability within the system. Visually, the most obvious timescale is associated with the  $O(10\text{ s})$  periods of surface waves. However, the nearshore spectrum often includes significant motions at longer scales such as infragravity waves (30–300 s periods) driven by wave groups (Herbers et al. 1995), very low-frequency motions (102–103 s periods) arising from current instabilities (Oltman-Shay et al. 1989), and longer timescales associated with system modulation by tides (Thornton and Kim 1993), and extreme events such as storms and hurricanes as well. Sand bars and bottom profile shapes evolve on timescales as short as days and force corresponding changes in the hydrodynamics. The 1–10 Hz sampling capability of most existing in situ sensors is adequate for high-frequency needs, but the requirement for extended sampling under difficult conditions usually leads to sensor degradation and excessive expense.

In the spatial domain, the nearshore is a region of high inhomogeneity. Surf zone motions and morphology are rarely uniform alongshore and so must also be sampled in the alongshore direction. Wave-breaking processes generally drive nearshore currents with similar spatial variability and induce sediment transport that creates nearshore sand bars, complex bottom morphologies, and eroding or accreting beaches. Wave motions, currents, and bathymetry all vary strongly over 10–1,000 m cross-shore scales. Proper sampling of this wide range of spatial scales would require a large array of in situ point sensors. In contrast, most remote sensors operate in an imaging mode that is optimized for such spatial sampling needs.

### ***7.1.2 Merits and Demerits Between Different Sensors***

Traditional in situ instruments such as buoys or bottom mounted pressure sensors can record precisely the variations of water surface elevations, velocities, sediment concentration, bottom elevation etc. with high sampling capability. These instruments are a powerful tool for monitoring nearshore regions. However, the measurements are expensive and limited in spatial extent. They must withstand wave forces, ocean currents, marine growth, and salt water immersion. In situ point sensors must be constantly monitored and regularly maintained to ensure their successful operation. Moreover, they require minimum depths to operate properly and are limited in study of nearshore processes. Further, during energetic sea states it is not easy to maintain data collection. Remote sensing techniques provide a

feasible alternative because they allow sampling over large spatial extents (meters to kilometers) and temporal scales (seconds to years).

Unlike in situ point sensors, remote sensing techniques provide a feasible alternative since they allow sampling over large spatial extents and temporal scales. Every digitized pixel in the remotely sensed area can be thought of as representing a “virtual” wave gauge. Methods of nearshore remote sensing include: Space-borne (satellite) radar, Synthetic Aperture Radar (SAR), High Frequency (HF) radar, X-band radar and Video Camera.

Space-borne radar and SAR remote sensing systems are limited by their ability to provide long term temporal information due to their lack of time on scene. Shore-based remote sensing systems, such as video and radar remote sensing systems can be set up at any coastal sites and offer much longer times on scene. Shore-based remote sensing systems avoid the problems associated with deployment and maintenance of in situ point sensors in the marine environment. Logistically there is minimal adjustment to the equipment for each individual deployment as the system is designed to function in a variety of environments. Deployment of shore-based remote sensing systems can typically be made in harsh weather without worry of damage to equipment or personnel.

Aerial photography is one of the earliest basic forms of remote sensing used to image wave fields over an area, and recently video cameras (e.g., Stockdon and Holman 2000; Plant and Holman 1997; etc.) or nautical radars (e.g., Bell 1999; Borge et al. 2004; Hasan and Takewaka 2007a, b etc.) have been employed for temporal coastal imaging supported by digital technologies and becoming popular for continuous monitoring.

For shore-based systems, e.g., a High-Frequency (HF) radar or X-band radar, the operation cost is relatively low, especially for the X-band radar if the required study area is within a radius of 3–5 km. HF radars are mainly used for large area currents and wave measurements (Gurgel et al. 1999). The principal for a HF and a X-band radar are same, all use Bragg effect to detect the scatter waves, but the selected wavelength are different. A HF radar selects large EM wavelength (with the frequency range from 3 to 30 MHz) to produce Bragg scatter waves with the gravity waves itself, but a X-band radar uses short EM waves to interact with ripples on top of the gravity waves. The operation range of HF radars is large (normally on the order of 50 km, and can be extended to 200 km with an antenna array) but with a relatively low resolution.

Video cameras can monitor sea surface patterns with high temporal resolution and can provide color images, which enable to detect wave breaking, suspension of foams, sediment concentrations etc. However, the spatial coverage is limited with a single camera, so deployment of multiple cameras is necessary to gain wide coverage. In addition, the use of video cameras is limited to daylight hours and fair atmospheric conditions.

Remote sensors often have the opposite problem of data starvation, i.e., too much data. For example, a single video camera can easily deliver  $35 \text{ MB S}^{-1}$ , and five cameras are commonly needed to span the full  $180^\circ$  field of view. Twelve hours of daylight would then yield 7.2 TB. Finally, remote sensing data are often surprisingly noisy. The presence of fog, low wind, or rain also contributes to data degradation.

**Table 7.1** Radar classifications (after Raemer 1996)

Band	Frequency	Wavelength
HF	3–30 MHz	10–100 m
VHF	30–300 MHz	1–10 m
UHF	300 MHz–1 GHz	30 cm–1 m
L-band	1–2 GHz	15–30 cm
S-band	2–4 GHz	7.5–15 cm
C-band	4–8 GHz	3.75–7.5 cm
X-band	8–12 GHz	2.5–3.75 cm
Ku-band	12–18 GHz	1.67–2.5 cm
K-band	18–27 GHz	1.11–1.67 cm
Ka-band	27–40 GHz	7.5 mm–1.11 cm
V-band	40–75 GHz	4–7.5 mm
W-band	75–110 GHz	2.7–4 mm
mm-band	110–300 GHz	1–2.7 mm

Some of the limitations of video imaging can overcome using X-band nautical radar. X-band nautical radar is an imaging tool that is capable of tracking movements of wave crests over large spatial regions and is becoming popular for coastal studies nowadays. The advantage in using an X-band radar system is its ability to monitor the coastal processes remotely and continuously, under calm conditions as well as stormy. Radar image sequences with large coverage (extending up to several kilometers) offer a unique opportunity to study individual waves and wave fields in space and time. The drawbacks of radars are their relatively low sampling rate and difficulties in detection of sediment suspensions and wave breaking states from the echo backscatter.

### 7.1.3 Basics of Radar Remote Sensing

Radar systems are classified by the wavelength of their emitted frequency. Marine radars are typically X- or S-band. Table 7.1 lists radar system classifications based on frequency and wavelength. Radar backscatter is produced from the interaction of electromagnetic (EM) waves and the rough surface of the ocean. The backscatter of the ocean surface is often called “Sea Clutter”. Electromagnetic energy is backscattered from the ocean surface by two general methods. Specular reflection is mirror-like reflection that is most predominant for small angles of incidence. The incidence angle is the angle that the incident ray makes with the normal to the surface. The grazing angle is complement of the incidence angle. In specular reflection the EM energy is reflected directly off the surface of the water. Bragg scattering is resonant reflection that occurs when EM energy interacts with waves that have a similar wavelength as the transmitted electromagnetic waves. Small scale capillary waves on the order of 1–3 cm provide the source for Bragg resonant scattering of marine X-band radars. Thus, the presence of wind is required to create these small scale waves in order for X-band radars to image ocean waves. The intensity of the backscattered energy is most affected by the magnitude of the wind

velocity, the incidence angle of the emitted EM energy, and the azimuth angle of the radar relative to the crest of the wave. Bragg scattering is strongest when the radar azimuth angle is aligned with the wave direction.

### **7.1.4 Swash Motion Studies**

Swash is the time varying position of the shoreward edge of water on a beach (e.g., Guza and Thornton 1985), and swash zone is the boundary between the inner surf zone and the sub-aerial beach (e.g., Ruggiero et al. 2004). Swash zone possesses scientific importance since significant amount of total surf zone sediment transport occurs within this region (Osborne and Rooker 1999). Swash zone hydrodynamics play a critical role in design and maintenance of shore protection structures as it is responsible for changing beach morphology by wave induced erosion or deposition (Ruggiero et al. 2001; Sallenger 2000). Despite this importance, there is still considerable debate as to how swash is related to environmental parameters such as the local beach slope or incident wave characteristics etc. Recent literature on swash zone processes (e.g., Elfrink and Baldock 2002; Butt and Russell 2000) highlights the lack of sufficient knowledge within this region.

Wave run-up is expressed as the set of discrete vertical elevations of seawater, measured on the foreshore from still water level (SWL) consisting of two components: a super elevation of mean water level, commonly known as wave setup, and vertical fluctuations about that mean. Many researchers investigated run-up dynamics on intermediate to reflective beaches (e.g., Holman and Sallenger 1985; Holman 1986; Holland and Holman 1999), low energy and mildly dissipative beaches (e.g., Guza and Thornton 1982; Raubenheimer et al. 1995; Raubenheimer and Guza 1996) and highly dissipative beaches (e.g., Ruessink et al. 1998; Ruggiero et al. 2004; Holman and Boyen 1984; Hasan and Takewaka 2009). Most of the studies parameterized wave run-up with environmental conditions and examined its relation with surf similarity parameter. However, there is still uncertainty on longshore propagation of the run-ups, particularly for the low frequency motions.

Miche (1951) hypothesized from laboratory observations that swash motion due to monochromatic waves generally saturated, and shoreline oscillation depends on wave frequency and beach slope. The saturation condition implies swash amplitude does not increase with increasing offshore wave height. Frequency components that are not dissipated and survive in the surf zone are reflected at the shoreline, and are relatively low frequency and have been termed as infra-gravity energy. Several studies have examined relative roles of the infra-gravity band run-up (generally  $f < 0.05$  Hz) and wind wave or incident band run-up ( $f > 0.05$  Hz) for particular field sites (e.g., Ruessink et al. 1998; Ruggiero et al. 2004; Hasan and Takewaka 2009 etc.). On natural beaches, run-ups at incident frequencies are typically saturated, while run-ups at infra-gravity frequencies are unsaturated and thus increases with offshore wave height (e.g., Guza and Thornton 1982; Holman and Sallenger 1985; Holland et al. 1995 etc.) and also depends on beach morphology (e.g., Hasan and Takewaka 2009). Extensive field evidence supports that energy at infra-gravity

frequencies often constitute a large portion of total energy observed at the shoreline during storm events (Holman 1981; Guza and Thornton 1982; Holman and Sallenger 1985; Raubenheimer and Guza 1996).

Holland and Holman (1999) examined wavenumber-frequency structure of swash variations over a range of environmental conditions using video technique with a 250 m longshore coverage. Frequency spectra of their analyses showed energy concentration at the infra-gravity band and wavenumber spectra were dominated by energy at low wavenumbers. Takewaka and Nishimura (2005) used X-band radar to analyze qualitatively longshore structure of swash motion during an energetic sea state. Recently, Hasan and Takewaka (2009) also analyzed wave run-up using X-band radar images during an energetic sea condition. They could be successful in tracing swash variations and its propagation in the longshore direction.

### ***7.1.5 Objectives of the Chapter***

Foreshore can be defined as the part of the shore, which is wet due to the varying tide and wave run-up under normal conditions. When ocean waves approach the shore, majority of the wave energy is dissipated across the surf zone through wave breaking. However, a portion of the energy is converted to potential energy in the form of run-up on the foreshore (Hunt 1959). This wave run-up is important to coastal engineers, nearshore oceanographers or coastal planners since run-up motions deliver most of the energy which is responsible for foreshore morphology such as dune and beach erosion (Ruggiero et al. 2001; Sallenger 2000) or beach cusp development (Inman and Guza 1982) etc. Hence, understanding the magnitude, longshore variability or propagation of wave run-up is critical to maintain the foreshore and its adjacent areas properly.

The deployment of a radar system is particularly advantageous over other measurement techniques for foreshore monitoring i.e. spatial analyses of run-up motions. Temporal and spatial variation of water front for a region can be observed with a single radar system. Using wave gauges to understand the spatial behavior of run-up will be extremely hard, laborious and expensive. Traces of water front and its motion can also be captured using video cameras with high temporal resolution; however, as mentioned above, at least several cameras are required in order to gain similar spatial coverage of a radar system.

An X-band radar system was operated at the research pier HORS (Hasaki Oceanographical Research Station, Fig. 7.1) at Hasaki beach, Japan for continuous nearshore monitoring since 2002. The present chapter analyzes radar echo images to estimate temporal and spatial variation of wave run-up, its spectral response, and dependence with foreshore slope during different storm events in 2005 over an extent of approximately 3.0 km. Radar echo images were collected for several hours during the passage of two typhoon events. Analyses on the echo images were done to evaluate longshore distribution of shoreline positions and inter-tidal foreshore slopes. Characteristics of the low frequency motions, its propagation and relation with different incident wave fields were analyzed and explained.

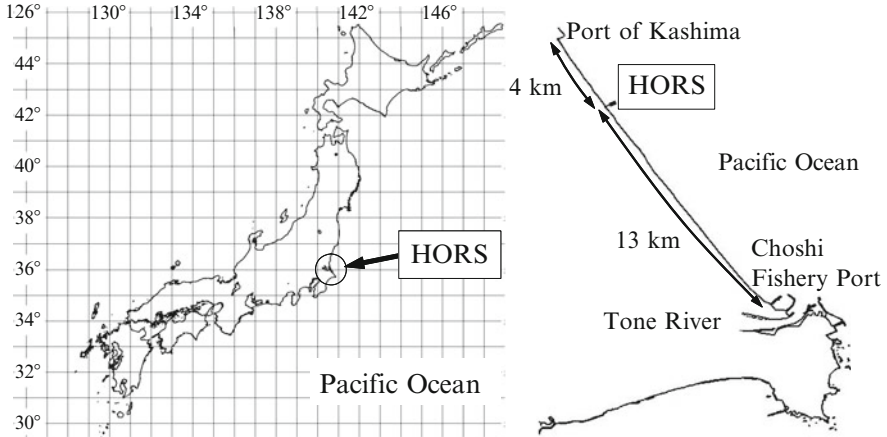


**Fig. 7.1** Location of the Hasaki Oceanographical Research Station (HORS) in Japan

Section 7.1 explains the importance of nearshore monitoring, merits and demerits between different sensors used for nearshore monitoring and objectives of this chapter. Setup of the study with incident wave field can be found in Sect. 7.2. Estimation of inter-tidal bathymetry and foreshore slopes using time-averaged radar images are explained in Sects. 7.3 and 7.4. Section 7.5 describes the estimation procedure of wave run-up with their validation, and formulate run-up with foreshore slope and surf similarity parameter. Concluding remarks based on the radar remote sensing are depicted in Sect. 7.6.

## 7.2 Setup of the Study

### 7.2.1 Research Pier HORS

X-band radar measurements were conducted at the research pier HORS of the Port and Airport Research Institute (PARI), located in Hasaki, Japan. Main facilities of the station are a 400 m long pier extending into the Pacific Ocean equipped with different in-situ measuring instruments and a research building located nearly 110 m back from the mean shoreline position. HORS is on an almost straight sandy coast approximately 17 km long with the Hasaki Fishery Port at the south end and Kashima Port at the north end of the coast (Fig. 7.1). The pier is located approximately 4 km away from Kashima Port. Water surface elevations are measured routinely with several wave gauges mounted on the pier and bottom profiles along the pier are surveyed on weekdays.

Moreover, airborne ultrasonic wave gauges were deployed in the swash zone with a close spacing along the pier for a few years (Mizuguchi and Seki 2007).



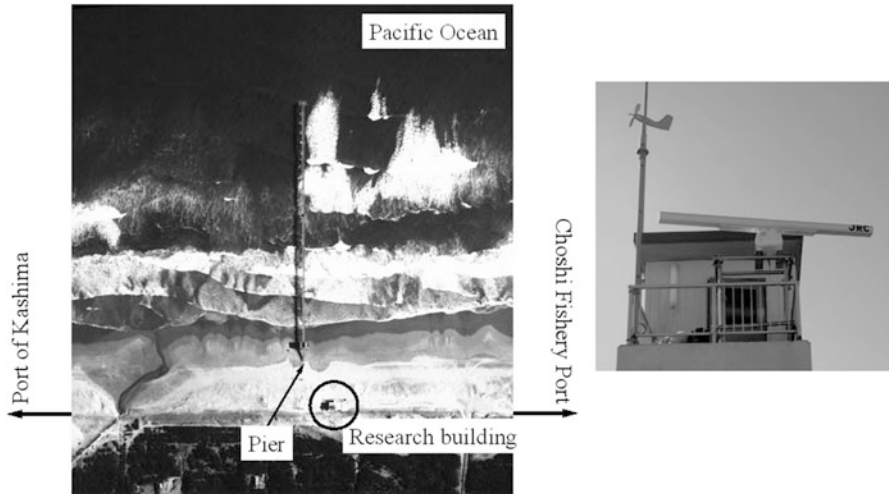


**Fig. 7.2** Aerial view of the Hasaki observation pier (*left photo*) and radar antenna (length ~2.8 m) on the roof of the research building (*right photo*). Length of the pier is approximately 400 m

Some gauges were installed well onshore around mean shoreline position to cope with large run-up during storm events. Wave gauges in the foreshore were placed with a small spacing (approximately 3 m). Wave gauges placed close to the shoreline are capable of measuring the elevation of the beach when it is bare during the swash-down phase as well as the water surface elevation when it is inundated during the swash-up phase. Thus the wave gauge system is capable of detecting the water front of the swash motion, and continuous measurements of both waves and beach profiles in the swash zone are possible.

### 7.2.2 Radar System and Echo Image

The radar system employed in this study is a conventional marine X-band radar, usually installed on fishing or recreational boats (Takewaka 2005; Hasan and Takewaka 2007a). The radar antenna (approximately 2.8 m in length, Fig. 7.2) is installed on the roof of the research building, which is 17 m above mean sea level. The figure also gives an aerial view of the HORS pier and its surrounding area. The antenna rotates with a period of approximately 2.5 s and transmits with a beam width of  $0.8^\circ$  horizontally and  $25.0^\circ$  vertically. The echo signals from the sea surface, generally called sea clutter, are captured with a specially designed A/D board installed on a computer. The backscatter echo signals are converted to gray images for further analyses.

Figure 7.3 shows the coordinate system used in this study. A sample radar image with reduced brightness is shown as a background in this figure. The  $x$ -axis

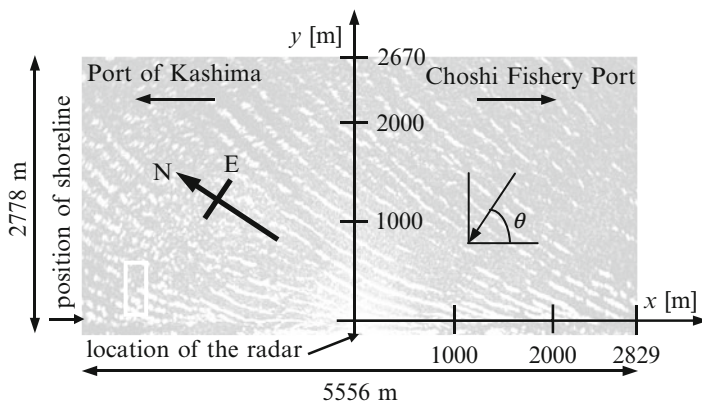


**Fig. 7.3** Coordinate system. Location of the radar is at  $(x, y) = (51, -108)$

corresponds to the longshore extent and positive towards the Choshi Fishery Port and the  $y$ -axis coinciding with the pier and oriented in the offshore direction. The figure also indicates the wave propagation direction  $\theta$ , with  $90^\circ$  being normal to the shore.

Measurements of the sea state using nautical radars are based on the backscatter of electromagnetic pulse from the sea surface. The echo signals from X-band radar were used to generate images with 1,024 pixels in horizontal and 512 pixels in vertical. The horizontal and vertical extents of an image correspond physically to a longshore extent of 5.6 km ( $\approx 3.0$  nautical miles) and a cross-shore extent of 2.8 km ( $\approx 1.5$  nautical miles), respectively, and each pixel corresponds to a square of 5.4 m. The gray images have pixel intensities between 0 (no backscatter) and 255 (highest signal).

The radar images were updated at every 2 s and its processing has been discussed in the author's previous work (Takewaka 2005; Hasan and Takewaka 2007a) in details. Figure 7.4 shows typical radar images captured during two storm events in 2005 having different incident wave field. The slanted white lines are oblique wave crests and the vertical white strip in the middle of the figure close to the bottom edge is the pier. Propagation of waves from different directions is observed from a sequence of radar images. The radar is located at the midpoint of the bottom edge of the diagram indicated by a black dot. Incoming waves mainly from a single direction is observed in the upper panel of Fig. 7.4, whereas waves propagation from multiple directions are shown in the lower panel of the figure.

### 7.2.3 Meteorological and Sea State Conditions

Typhoon BANYAN (Typhoon #7, T7 in 2005) traveled through the western edge of the Pacific Ocean from 21st to 31st of July. Also, typhoon SAOLA (Typhoon #17, T17 in 2005) followed almost similar track in the Pacific Ocean and traveled from 20th to 26th of Sept. Tracks of both the typhoons can be obtained from the authors'

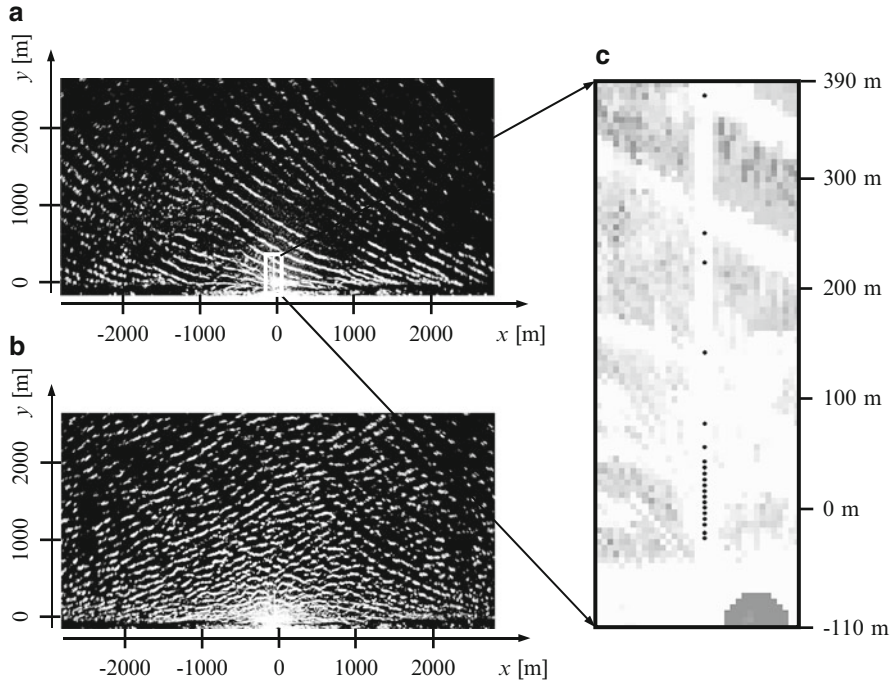


**Fig. 7.4** Typical radar echo image during the period of (a) typhoon BANYAN (typhoon # 7, T7,  $H_s=3.69$  m and  $T_s=12.1$  s) and (b) typhoon SAOLA (typhoon # 17, T17,  $H_s=4.87$  m and  $T_s=9.6$  s) in 2005. Close up view of an echo image showing wave gauge locations (*black dots*) along the pier (c)

previous studies (Hasan and Takewaka 2007a, b). Radar echoes were collected continuously for several hours during the passage of the typhoon events and used for these analyses.

Atmospheric pressure is recorded by the Japanese Meteorological Agency (JMA) at the Choshi Fishery Port. Analyzing periods for both the storm events were selected, when the lowest atmospheric pressure was closest to the HORS, which is 22nd hour of Jul 26 during typhoon BANYAN and 14th hour of Sept 25 during typhoon SAOLA. Wind speed and its direction are also collected from JMA. Wind was found weak during 2005/Jul/26/22 h, whereas strong north-eastern wind ( $\sim 23.5$  m/s) was blowing over this region during 2005/Sept/25/14 h which was induced by the typhoon SAOLA.

Offshore waves were measured by the Nationwide Ocean Wave Information Network for Ports and Harbors (NOWPHAS, [http://infosv2.pari.go.jp/bsh/ky-skb/kaisho/eng/marine\\_home\\_e.htm](http://infosv2.pari.go.jp/bsh/ky-skb/kaisho/eng/marine_home_e.htm)) station near the Kashima Port. Table 7.2 summarizes the sea state conditions during the analyzing periods obtained from NOWPHAS record. The local datum level (DL) defined at HORS used in this study which is 0.687 m below the datum level of Tokyo Peil (TP) usually used in Japan.

**Table 7.2** Sea state conditions during the analyzing hours estimated by NOWPHAS (at Kashima Port)

Parameters	2005/Jul/26/22 h	2005/Sept/25/14 h
Significant wave height $H_s$	3.69 m	4.87 m
Significant wave period $T_s$	12.1 s	9.6 s
Significant wave direction $\theta_s$	33°	89°
Tide level	1.21 m	1.39 m

**Table 7.3** Estimated wave heights and directions for different frequency bins by NOWPHAS during typhoon BANYAN (2005/Jul/26/22 h) and typhoon SAOLA (2005/Sept/25/14 h)

Frequency [Hz]	2005/Jul/26/22 h		2005/Sept/25/14 h	
	Wave height [m]	Wave direction [deg]	Wave height [m]	Wave direction [deg]
<0.03125	0.31	Not estimated	0.92	Not estimated
0.04~0.0625	1.73	39	0.95	60
0.0704~0.0935	2.86	38	2.55	88
0.102~0.125	1.23	47	2.5	110
0.133~0.2325	1.34	51	2.54	123
>0.244	0.80	Not estimated	1.10	Not estimated

Sequences of radar images exhibit propagation direction of the incoming waves. Single dominant oblique direction was observed from the wave field during typhoon BANYAN (2005/Jul/26/22 h), whereas incoming waves from several directions were observed from the wave field generated by typhoon SAOLA (2005/Sept/25/14 h). Wave heights and wave directions of different frequencies for the analyzing hours are summarized in Table 7.3 which was processed by NOWPHAS at Kashima Port. Propagations of different frequency waves from different directions were observed during 2005/Sept/25/14 h which can be observed from the table, whereas almost single incoming waves were found during 2005/Jul/26/22 h.

### 7.2.4 Spectral Characteristics of Incident Wave Fields

Offshore wave field during the period of typhoon BANYAN (2005/Jul/26/22 h) were analyzed by Hasan and Takewaka (2007a) using X-band radar images. Temporal variations of echo signals were analyzed with the Fast Fourier Transform (FFT) to examine the dominant frequency wave. A sequence of images of 256.0 s (128 images) was used in the analysis and the peak frequency corresponding to the highest spectral density was determined. Spectrum along a cross-shore line  $y = 1,000$  m is shown in the upper panel of Fig. 7.5a which is normalized and alongshore averaged. Peak frequency  $f_p$  of 0.066 Hz ( $\sim 15.1$  s) is apparent in the spectrum. The lower panel of Fig. 7.5a shows the results of the FFT analyses along the cross-shore displayed as an image view. Spectra were prepared in the same manner as described above. The brightness of the image corresponds to higher spectral strength. The figure depicts the

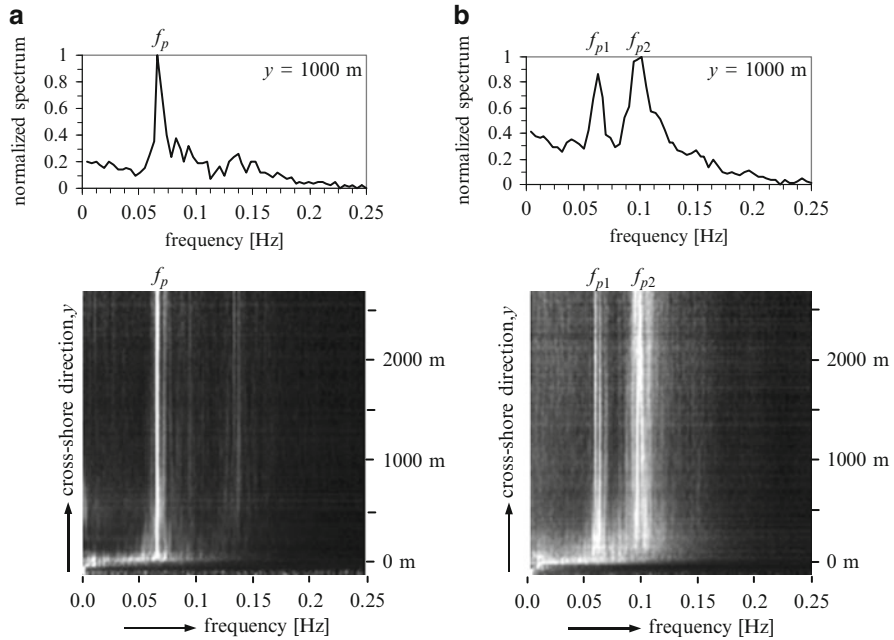


**Fig. 7.5** Frequency spectra of the incident wave field for the period of (a) typhoon BANYAN (2005/Jul/26/22 h) and (b) typhoon SAOLA (2005/Sept/25/14 h) (From Hasan and Takewaka 2007a, b). Brighter intensities in the lower images correspond to higher spectral strength

cross-shore uniformity of the peak frequency  $f_p$  0.066 Hz, which shows dominance of a single wave component during this period.

Temporal variations of radar echo signals were also analyzed with the FFT for the period of typhoon SAOLA (2005/Sept/25/14 h) by Hasan and Takewaka (2007b). A sequence of images of 512.0 s (256 images) was used in the analysis and peak frequencies corresponding to higher spectral strength were determined. Spatially averaged spectra at a cross-shore coordinate  $y = 1,000$  m is shown in the upper panel of Fig. 7.5b which was processed similarly as described above. Two distinct peaks  $f_{p1}$  and  $f_{p2}$  are observed in the spectrum. The higher frequency component ( $f_{p2} = 0.095$  Hz) is predominant over the other one ( $f_{p1} = 0.0625$  Hz). Lower panel of Fig. 7.5b shows the results of the FFT analyses displayed as an image view. The figure shows almost uniformity of the spectral structure in the cross-shore direction. Energetic waves at higher frequency range (0.133 ~ 0.2325 Hz) is observed by NOWPHAS as shown in Table 7.3, which is not resolved in the spectra estimated using radar images. Since this frequency range is close to the Nyquist frequency of radar measurement (0.25 Hz for this analysis), the radar system failed to catch these waves.

In the followings, longshore structures of the run-up motion were analyzed and compared between different incident wave fields, namely 22 h of 2005/Jul/26 as a wave field with dominant single wave incidence and 14 h of 2005/Sept/25 as a wave field with multiple wave incidences.

## 7.3 Implication of Averaged Images

### 7.3.1 *Inter-tidal Bathymetry*

Inter-tidal foreshore profiles (i.e., bathymetry, foreshore slope etc.) were estimated by analyzing time-averaged images of different tide levels between high and low tide bands as the same manner of Takewaka (2005) for both the typhoon periods. Sequence of individual echo images were averaged to yield a time-averaged image or so called time-exposure image. Figure 7.6 shows images averaged over 17 min (512 images) during a high tide and a low tide observed under stormy conditions on 2005/Jul/26 (typhoon BANYAN period) and also on 2005/Sept/25 (typhoon SAOLA period). Individual waves vanish in the time-averaged images, and a horizontal edge corresponding to the shoreline appears as shown in Fig. 7.6.

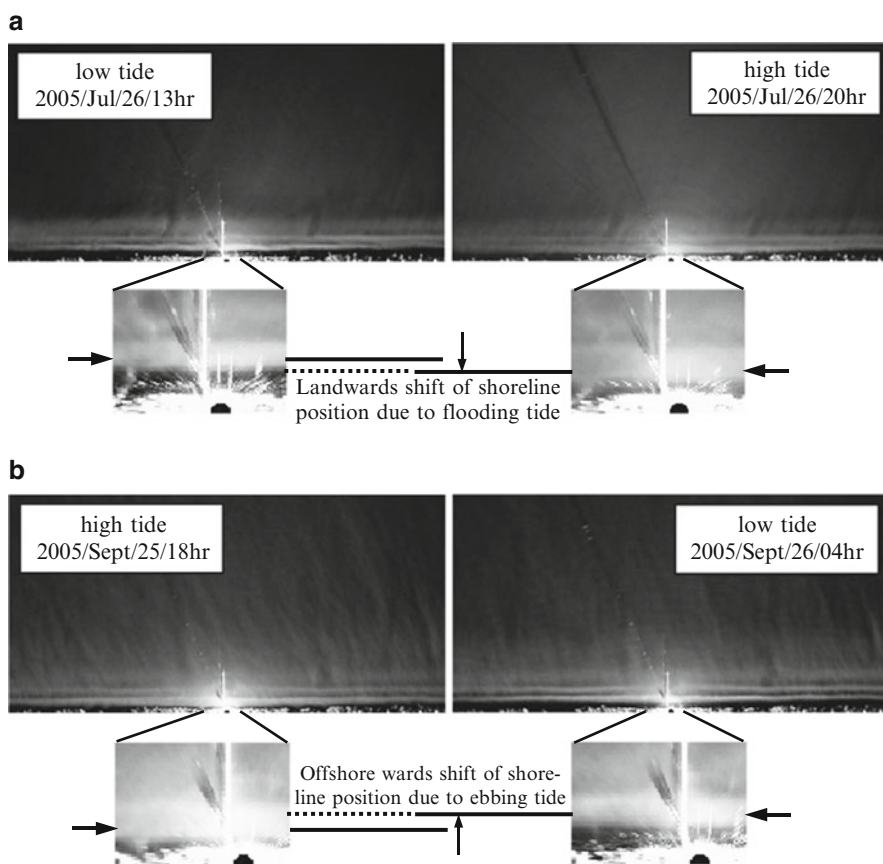


**Fig. 7.6** Averaged images at low tide and high tide condition for the period of (a) typhoon BANYAN (T7) and (b) typhoon SAOLA (T17) in 2005. Series of averaged images within this low tide and high tide band was used to estimate the foreshore profile

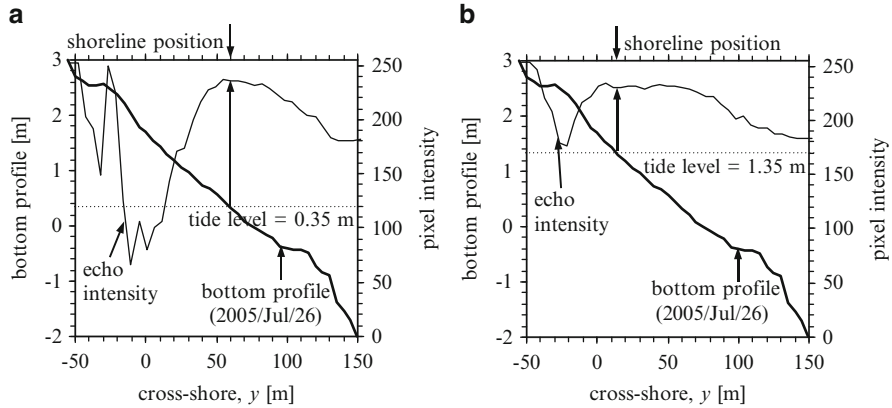


**Fig. 7.7** Cross-shore pixel intensities extracted from time-averaged images at  $x = -47$  m displayed with the bottom profile along the pier ( $x = 0$ ) during (a) low tide (2005/Jul/26/13 h) and (b) high tide (2005/Jul/26/20 h) condition for the period of typhoon BANYAN

A close-up view around the pier is included in this figure in which shifting of shorelines due to changing tide levels are clearly visible.

Pixel intensities extracted along a cross-shore line from time-averaged images are shown in Fig. 7.7 along with the tidal elevation and bottom profiles. Location of the broad peak in the echo intensity variation coincides with the position of the intersection of the tidal elevation and bottom profiles, which is the shoreline position (i.e., Takewaka 2005). Thus the shorelines can be determined by locating peaks in the cross-shore pixel intensity distribution.

For the estimation of foreshore profile, horizontal position of the shoreline was determined from radar measurements, and vertical position was taken from corresponding tide records. A period of large tidal changes was chosen for the inter-tidal bathymetry preparation to obtain a wide coverage for the particular analyzing periods of run-up observations. During typhoon BANYAN, 2005/Jul/26/13 h as low tide (tide level: 0.348 m) and 2005/Jul/26/20 h as high tide (tide level: 1.348 m) were considered as the inter-tidal band. Similarly, inter-tidal range between 2005/Sept/25/18 h (as high tide, tide level: 1.578 m) and 2005/Sept/26/04 h (as low tide, tide level: 0.598 m) was chosen for the estimation during the other typhoon period. Tide levels recorded by the JMA at the Choshi Fishery Port are shown in Fig. 7.8 with indication of inter-tidal range used for the profile estimation. Shoreline positions were digitized manually from hourly time-averaged images within the inter-tidal band. Then parabolic curves were fitted for the shoreline positions with the help of corresponding tidal elevations. The estimated bathymetries from radar measurements close to the pier ( $y = -47$  m) are depicted in Fig. 7.9, which agrees reasonably well with the results of the bathymetric survey along the pier ( $y = 0$  m). Note that  $x = -47$  m is the nearest available position from the radar measurements which is the reason for the horizontal shift of the comparison. Foreshore profile has been changed between the two typhoon events which can be observed from the comparison.



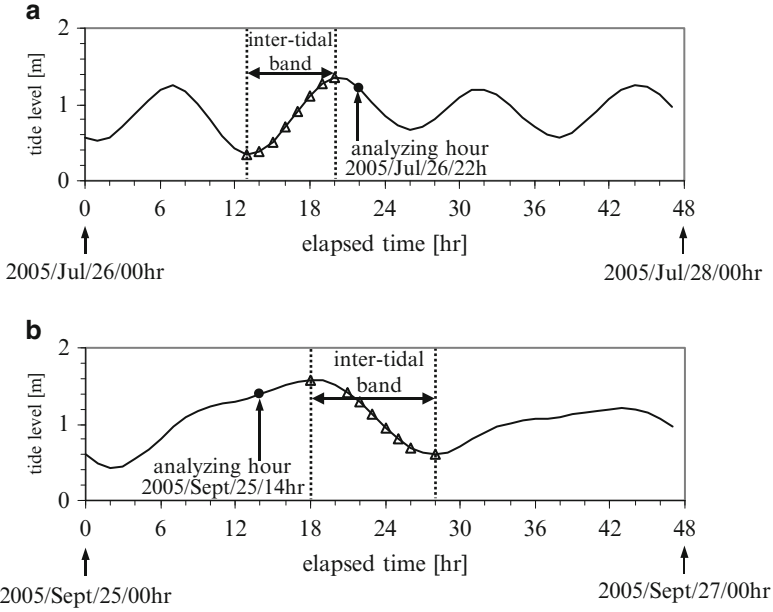


**Fig. 7.8** Tide records at Choshi Fishery Port measured by the Japan Meteorological Agency (*JMA*) during (a) typhoon BANYAN (T7) and (b) typhoon SAOLA (T17). Dotted lines indicate the inter-tidal range used for estimating foreshore profiles and also open symbols indicate the periods considered for digitization of the time-averaged images

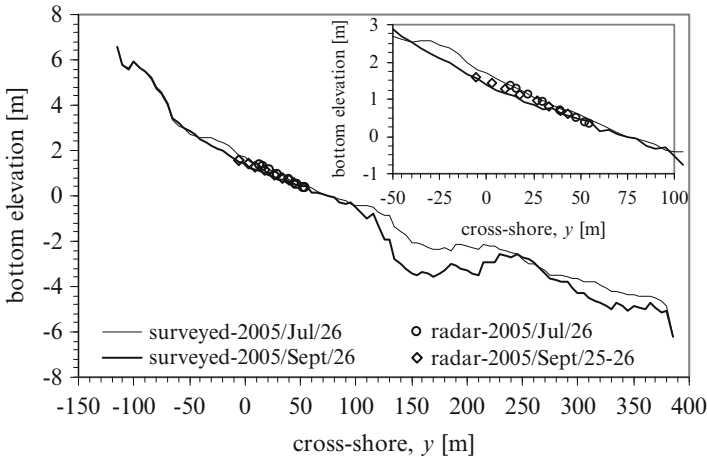


**Fig. 7.9** Comparison of bottom profiles between radar measurements ( $x = -47$  m) and surveyed results along the pier ( $x = 0$  m) for both the typhoon periods (e.g., typhoon BANYAN: 2005/Jul/26 and typhoon SAOLA: 2005/Sept/25–26)



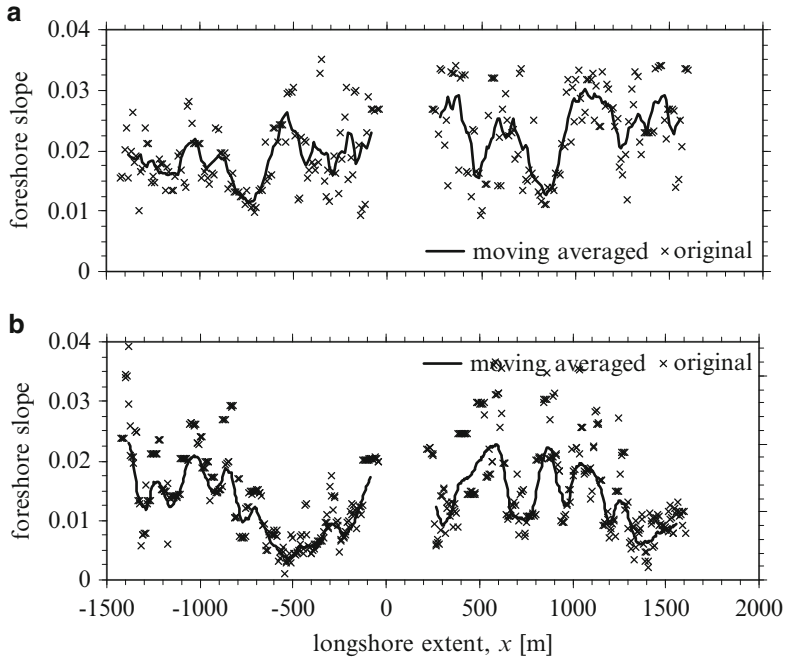


**Fig. 7.10** Longshore variation of foreshore slope for the period of (a) typhoon BANYAN (2005/ Jul/26/22 h) and (b) typhoon SAOLA (2005/Sept/25/14 h)

### 7.3.2 Foreshore Slope

Foreshore slopes were estimated from the fitted foreshore profiles as the same manner of Hasan and Takewaka (2009). Mean foreshore slope is defined at every longshore position from average of foreshore slopes at three cross-shore locations – swash-up, swash-down and mean swash position (locations are explained in the next section). The foreshore slopes at those locations were estimated from the results of the parabolic curve fitting applied to the digitized inter-tidal foreshore profile. Longshore distributions of the mean foreshore slopes are shown in Fig. 7.10, where symbols indicate the original variation and continuous lines indicates moving average of them with an averaging width of 86.8 m. A wavy structure with length of order of 500 m along the shoreline configuration is observed. Longshore-averaged foreshore slope during typhoon BANYAN (2005/ Jul/26/22 h) is 0.022 ( $\sim 1/45$ ), while the foreshore slopes varied from 0.011 to 0.03 over the area. The estimated foreshore slopes also varied from 0.004 to 0.033 for the other typhoon period (2005/Sept/25/14 h) with milder longshore-averaged slope 0.0125 ( $\sim 1/80$ ).

## 7.4 Swash Front Analyses

### 7.4.1 Digitization of Swash Motion

Pixel intensities along a cross-shore line are extracted from a sequence of echo images and stacked in time to produce a cross-shore time stack image. Time stack is a composite image whose one axis represents time and coastal extent is the other axis. Local gradients of the oblique white streaks in the time stack image correspond to wave propagation speeds in the cross-shore direction. Changes in local inclinations of these lines in the vicinity of the shore reflect retardation of wave celerity during shoaling, and merging of waves occurs at intersections of the lines in the swash zone. Lower end points of the lines are the maximum swash points, which fluctuate in time suggesting that low frequency motion exists in the swash zone. Landward most identifiable edge of water, which is the boundary between land and water, was determined by manual digitization of the cross-shore time stack images. Series of time stack images was prepared at 256 transects for the period of typhoon BANYAN (2005/Jul/26/22 h) and at 512 transects for the period of typhoon SAOLA (2005/Sept/25/14) with time duration of 1024.0 s. Examples of digitized stacks are shown in Fig. 7.11 which reveal large scale up and down variation in time.

The digitization was done by tracking the up-rush of individual waves from offshore points up to the swash peaks and subsequent down-rush. Unfortunately, the down-rush is less distinct and not able to detect clearly from the time stack

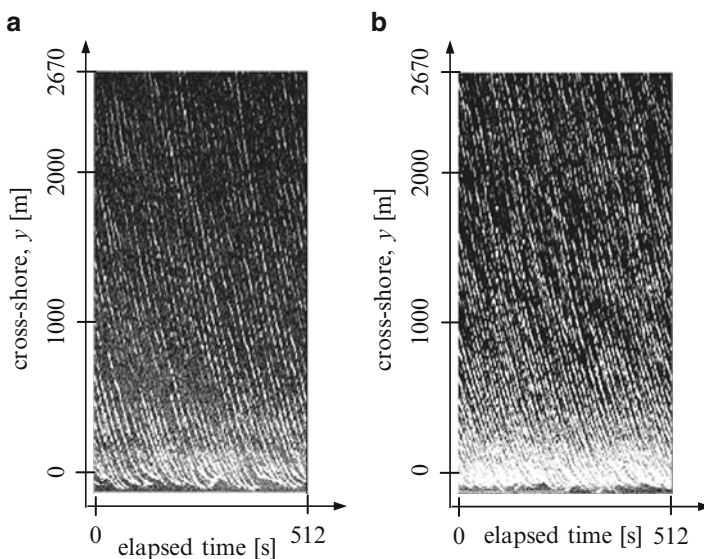


**Fig. 7.11** Cross-shore time stack images for the period of (a) typhoon BANYAN (2005/Jul/26/22 h) and (b) typhoon SAOLA (2005/sept/25/14 h) at  $x = -166$  m

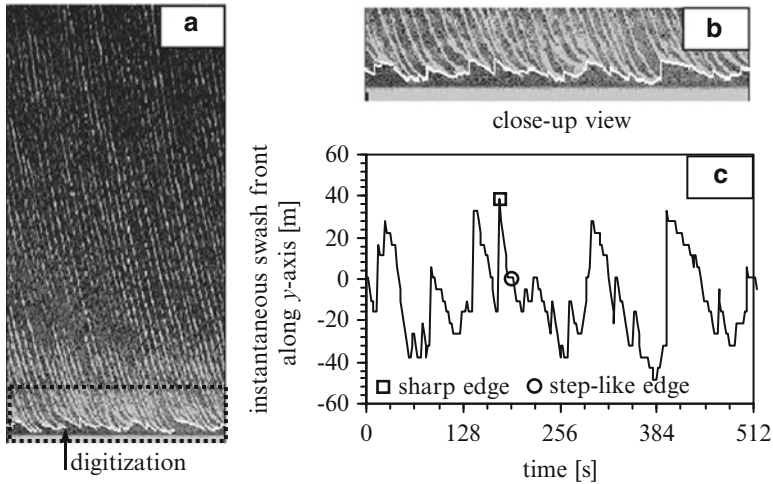


**Fig. 7.12** (a) Manual digitization of the swash front, (b) close-up view of the digitization process, and (c) time variation of instantaneous swash front  $S$  at a cross-shore transect ( $x = -166$  m) during high tide condition (2005/Jul/26/22 h). Open symbols on (c) are indicating a sharp and a step-like edge

images, which is a limitation of radar measurements and explained in Hasan and Takewaka (2009) in details. An example of a digitized stack is depicted in Fig. 7.12a with a close-up view in Fig. 7.12b and a variation of digitized swash front  $S(x, t)$  in Fig. 7.12c. The swash front shows large scale up and down variation with an amplitude of approximately 50 m. Sharp edges probably appeared during manual digitization from not following the actual down-rush pattern. Step-like edges also become visible in the variation, most likely due to the non-updated parts of the image sequence. Figure 7.12c depicts a sharp and a step-like edge with open symbols as an example. Troughs in the variation curve are defined as individual swash-ups correspond to run-up positions, whereas peaks are termed as individual swash-downs.

Extreme values (troughs in  $S$ ) located further land-wards than the temporal mean of the swash variation at a cross-shore transect were identified as swash-ups. Swash-downs were also estimated in a similar manner from extreme values (peaks in  $S$ ) located further offshore-wards than the temporal mean. The positions of swash-up, swash-down and mean swash  $S_m$  at each cross-shore transect were used to estimate foreshore slope as explained in the previous section.

#### 7.4.2 Validation of Swash Front

The digitization of the swash motion is dependent on the subjective judgments of the individual operators. Accuracy of the digitization was checked by comparison with in situ measurements. A number of wave gauges were placed along the pier to observe

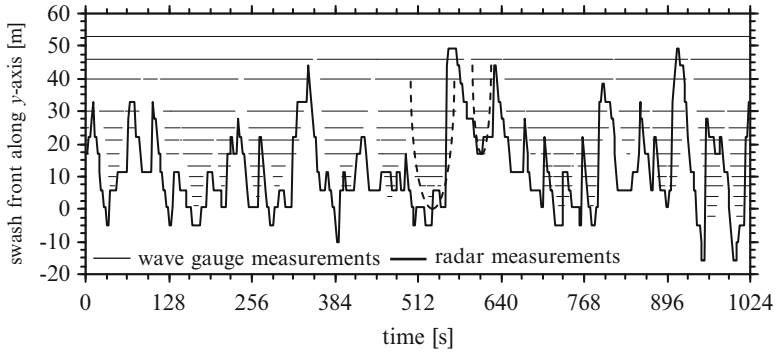


**Fig. 7.13** Comparison between swash front  $S$  digitized from X-band radar images at  $x = -47$  m and water traces detected with ultra-sonic wave gauge system at  $x = 0$  m (along the pier) during a low tide (2005/Jul/27/02 h, tide level: 0.66 m). Wave gauge measurements (*horizontal lines*) are displayed at the location of gauges, whose positions are shown in Fig. 7.3c. Dotted parabolas are schematically drawn the up-rush and down-rush pattern of the wave gauge records

run-up fluctuations during the typhoon BANYAN as explained in Sect. 7.2.1. The location of the gauges are shown in Fig. 7.4c with the most landward one placed at  $y = -23$  m. The digitized water-front variations  $S$  at  $x = -47$  m were compared with wave gauge records at  $x = 0$  m as shown in Fig. 7.13.  $x = -47$  m is the nearest available position from the digitization which is the reason for the horizontal shift of the comparison. The horizontal lines in the figure represent the times and places where water was detected by the wave gauge system. The overall comparison of the water fronts detected by both systems shows an acceptable agreement, particularly for up-rush patterns. Smooth down-rush patterns can be identified from the wave gauge records, whereas the variation is somewhat abrupt for radar estimates, resulting in discrepancies in the swash-down phases.

It is widely accepted that the pattern of up-rush and down-rush of the waterfront can be approximated with a parabola (e.g., Shen and Meyer 1963), and this is observed from the wave gauge record in Fig. 7.13; however the digitized swash front is a bit skewed due to its less distinctive swash-down pattern. Since the down-rush pattern of the radar measurements does not follow an actual parabolic path and the digitization was down by jumping to the next wave at an offshore location from the swash peak, a small offshore-ward shift of the digitized swash-down position from its actual position occurs.

### 7.4.3 Shoreline Position

The instantaneous swash variation  $S$  at  $x = -47$  m is displayed along with a surveyed bottom profile along the pier ( $x = 0$  m) in Fig. 7.14 to cross check the accuracy of the digitized swash. Temporal mean of the swash variation  $S_m$  should close to the shoreline position, which can also be determined from the intersection

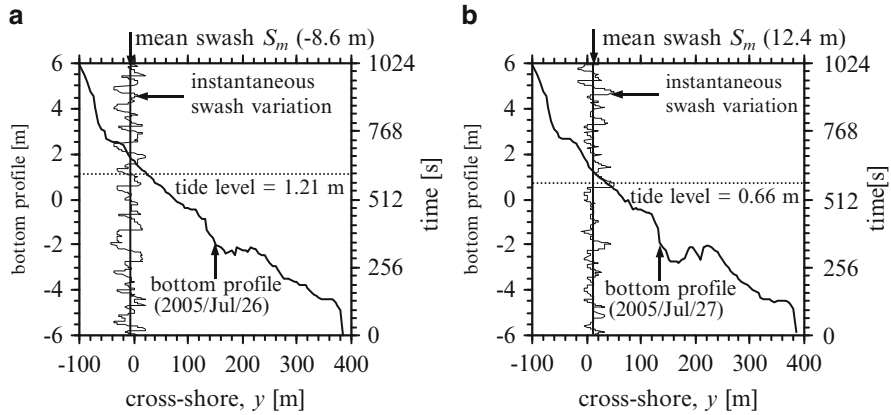


**Fig. 7.14** Bottom profile along the pier ( $x=0$ ) displayed with time variation of instantaneous swash front  $S$  close to the pier ( $x=-47$  m) during (a) high tide (2005/Jul/26/22 h) and (b) low tide (2005/Jul/27/02 h) condition

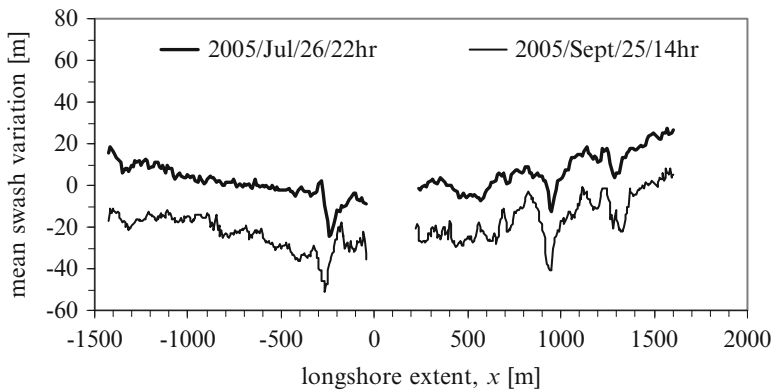


**Fig. 7.15** Comparison between longshore distribution of mean swash  $S_m$  for the period of typhoon BANYAN (2005/Jul/26/22 h, tide level = 1.21 m) and typhoon SAOLA (2005/Sept/25/14 h, tide level = 1.39 m)

of the surveyed bottom profile and tide level (as explained through Fig. 7.7). Figure 7.14 also plotted simultaneously mean swash  $S_m$ , tide level and bottom profile. Small discrepancy between the mean swash and the shoreline position defined from the bottom profile is observed, which probably arises from two sources: (i) the mean swash determined from the radar data includes wave setup at the shoreline, whereas the measured tidal elevation does not, and (ii) a horizontal shift of 47 m between the points of comparison.

Longshore distribution of mean swash variation  $S_m(x)$  is shown in Fig. 7.15. The figure compares  $S_m$  between the period of typhoon BANYAN (2005/Jul/26/22 h)

and typhoon SAOLA (2005/Sept/25/14 h). The mean position is gradually shifting landward towards the pier in negative longshore locations, whereas wavy distribution is observed in positive longshore locations and the pattern is almost similar in both the periods. Cross-shore transition of the shoreline position observed from the figure is basically due to difference of the tide levels, which is 1.39 m during 2005/Sept/25/14 h and 1.21 m during 2005/Jul/26/22 h.

## 7.5 Longshore Structure of Wave Run-up

### 7.5.1 Run-up Height

Pixel intensities along a cross-shore transect are extracted from a sequence of echo image and stacked in time to produce a cross-shore time stack image. Cross-shore time stack, a composite image whose one axis represents time and cross-shore extent is the other, is useful to understand maximum swash positions and its fluctuation in time. Landward most identifiable edge of water, i.e., the boundary between land and water, was determined by manual digitization of the time stack images. Series of cross-shore time stack images in alongshore direction were digitized to examine the longshore structure of the low frequency run-up motion.

Time stack images were digitized at 256 longshore locations with an interval of 10.85 m (2 pixel spacings) for the period of typhoon BANYAN (2005/Jul/26/22 h), whose first half falls in the negative longshore region ( $-1425 \text{ m} < x < -47 \text{ m}$ ) and rest in the positive region ( $225 \text{ m} < x < 1,603 \text{ m}$ ). Longshore coverage by all 256 transects is approximately 3.0 km. For the period of typhoon SAOLA (2005/Sept/25/14 h), time stack images were digitized with a similar manner at 512 longshore locations with an interval of 5.42 m (1 pixel spacing). Longshore coverage by all 512 transects are  $-1,425 \text{ m} < x < -41 \text{ m}$  and  $219 \text{ m} < x < 1,603 \text{ m}$ . The gap of the digitization ( $-36 \text{ m} < x < 214 \text{ m}$ ) in front of radar is due to avoid signal saturation, which was difficult to digitize and this study neglects this region for subsequent analyses. Digitized swash fronts  $S(x, t)$  during the analyzing periods are displayed in Fig. 7.16 along the cross-shore transect  $x = -166 \text{ m}$ .

Swash fluctuation digitized from cross-shore time stack images at each transect and were converted to vertical elevation with the help of foreshore profile. Time history of the estimated water front elevation  $R_f$  at a cross-shore transect  $x = -166 \text{ m}$  is shown in the upper panel of Fig. 7.17. Still water level (SWL) is considered as the position of tidal elevation and its level is also shown in the same figure. The vertical elevation basically consists with two components: a super elevation known as wave setup which is the mean of the estimated elevation, and fluctuation about that mean. Statistical analyses of the time history of estimated elevation and their comparison between the two analyzing periods were done and discussed in the following sections.

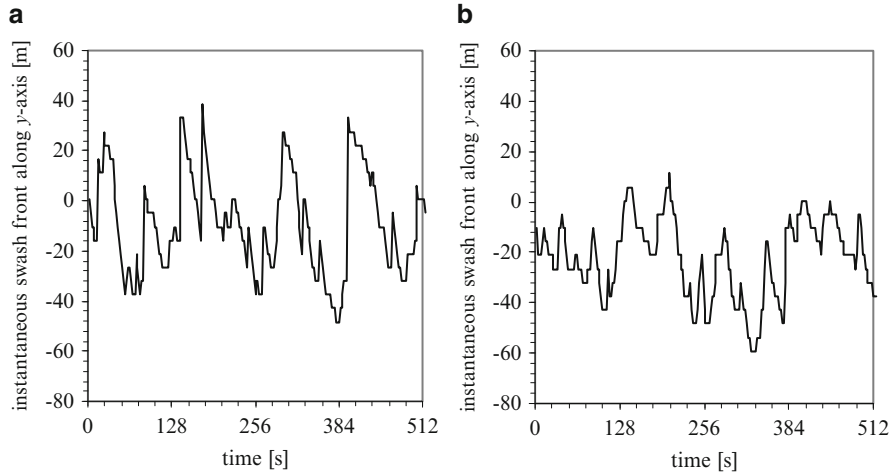


**Fig. 7.16** Time variation of digitized swash front  $S$  for the period of (a) typhoon BANYAN (2005/Jul/26/22 h) and (b) typhoon SAOLA (2005/Sept/25/14 h) at a cross-shore transect  $x = -166$  m

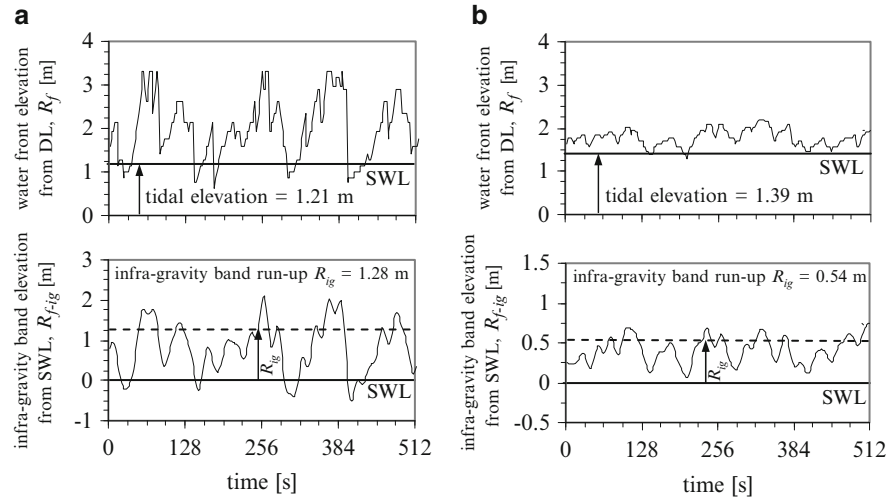


**Fig. 7.17** Time variation of water front elevation  $R_f$  measured from datum level (DL) for the period of (a) typhoon BANYAN (2005/Jul/26/22 h) and (b) typhoon SAOLA (2005/Sept/25/14 h) at  $x = -166$  m. Bottom panel shows the filtered infra-gravity band elevation  $R_{f-ig}$  with respect to still water level (SWL).  $R_{f-ig}$  variation was used to estimate the infra-gravity band run-up  $R_{ig}$

### 7.5.2 Infra-gravity Run-Up Distribution

Energy in the incident and infra-gravity frequency bands generally contributes varying amounts of total run-up (e.g., Guza and Thornton 1982) and therefore separation into two bands is required. In order to check the relative role of the

infra-gravity band run-up variation, the water front elevations  $R_f$  were band pass filtered with frequency range of  $0.004 < f < 0.05$  Hz. The separation frequency used for filtering the infra-gravity variation is somewhat subjective, which was also chosen by several researchers for run-up analyses (e.g., Holland and Holman 1999; Ruessink et al. 1998; Ruggiero et al. 2004; Hasan and Takewaka 2009 etc.). The reference level of the water front elevations was then shifted to still water level for run-up analyses. Time histories of the filtered infra-gravity band run-up variations  $R_{f-ig}$  along  $x = -166$  m are shown in lower panel of Fig. 7.17. Hasan and Takewaka (2009) analyzed the relative contribution of both the infra-gravity band and incident band run-up during typhoon BANYAN. They observed that energy of infra-gravity band run-up was dominant and energy of incident band was negligible.

Run-up heights of the infra-gravity band  $R_{ig}$  at each transect was estimated from the time history of  $R_{f-ig}$  variation as the same manner of Hasan and Takewaka (2009). Mean of the discrete local maxima above still water level in the  $R_{f-ig}$  variation is defined as  $R_{ig}(x)$ . Longshore distribution of the  $R_{ig}$  is shown in Fig. 7.18, where the crosses indicate the original estimates and the solid line indicates moving average of the estimates with an 86.8 m averaging width (nine grid spacing during 2005/Jul/26/22 h and 17 grid spacing during 2005/Sept/25/14 h). The figure simultaneously shows the distribution of the foreshore slopes for both the periods.  $R_{ig}$  has a tendency to be relatively high in regions where the foreshore slopes are steep and vice versa. Longshore distributions of  $R_{ig}$  were ranging from 0.33 to 1.67 m and from 0.37 to 1.78 m, for the period of typhoon BANYAN (2005/Jul/26/22 h) and typhoon SAOLA (2005/Sept/25/14 h), respectively.

### 7.5.3 Spectra of Water Front Elevation

Spectra of the water front elevation  $R_f$  was estimated at each cross-shore transect using the Fast Fourier Transform (FFT). Data length and interval for the spectra estimation were 1024.0 s and 2.0 s. The estimated spectra were alongshore averaged and depicted in Fig. 7.19. Single peak frequency of 0.0078 Hz (128.0 s) corresponding to highest spectral density is observed in the spectrum for the period of typhoon BANYAN (2005/Jul/26/22 h), whereas two dominant peaks of 0.0078 Hz (128.0 s) and 0.0107 Hz (93.1 s) are observed for the period of typhoon SAOLA (2005/Sept/25/14 h). Spectral characteristics of the water front elevations resemble the spectra of the incident wave field for both periods.

Frequency spectra of the offshore wave field for the period of typhoon BANYAN (2005/Jul/26/22 h) show dominant waves with 15.1 s period (0.066 Hz) were approaching towards shore, whereas two dominant waves with 16.0 s (0.0625 Hz) and 10.5 s (0.095 Hz) were observed from the frequency spectra for the period of typhoon SAOLA (2005/Sept/25/14 h). Energies of these incident waves are not found in the  $R_f$  spectra for both the periods, suggesting a saturated condition of the incident waves.



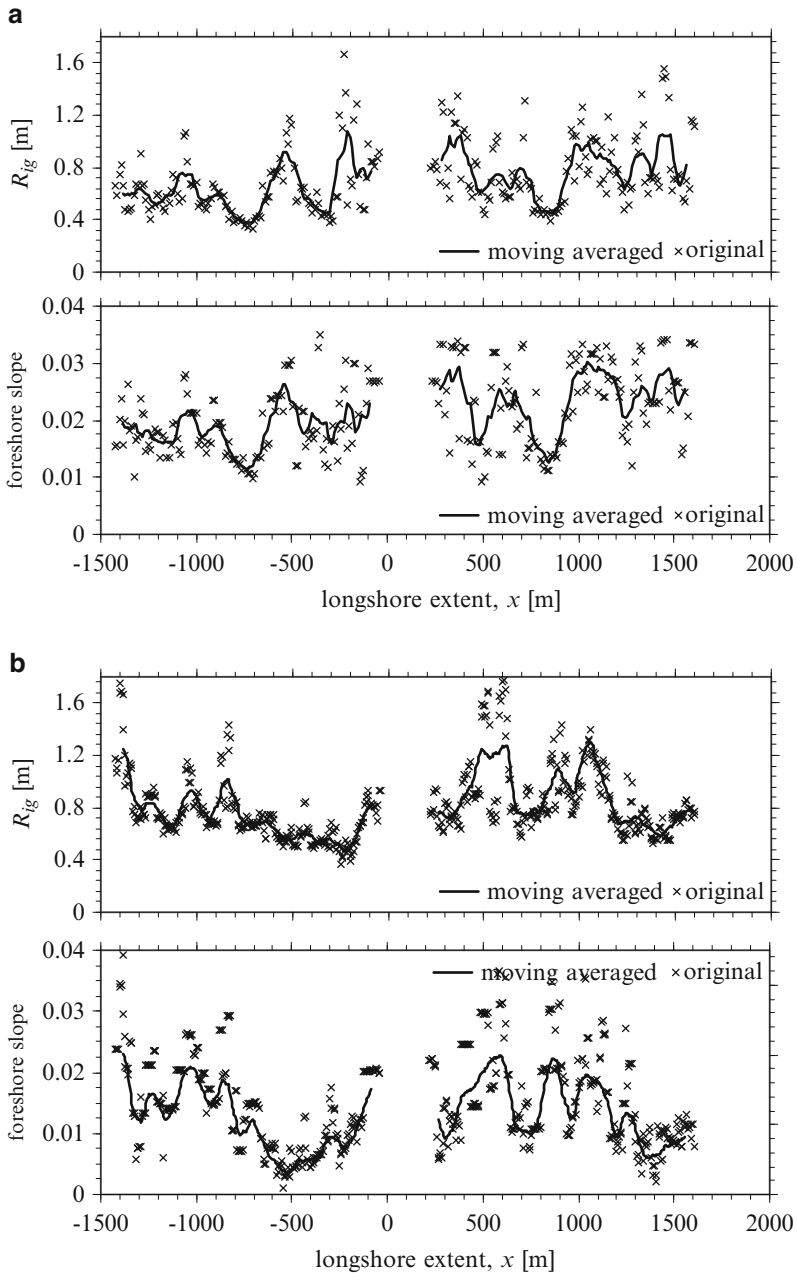


**Fig. 7.18** Longshore distribution of infra-gravity band run-up  $R_{ig}$  with corresponding foreshore slope for the period of (a) typhoon BANYAN (2005/Jul/26/22 h:  $H_s = 3.69$  m,  $T_s = 12.1$  s, tide level = 1.21 m) and (b) typhoon SAOLA (2005/Sept/25/14 h:  $H_s = 4.87$  m,  $T_s = 9.6$  s, tide level = 1.39 m)

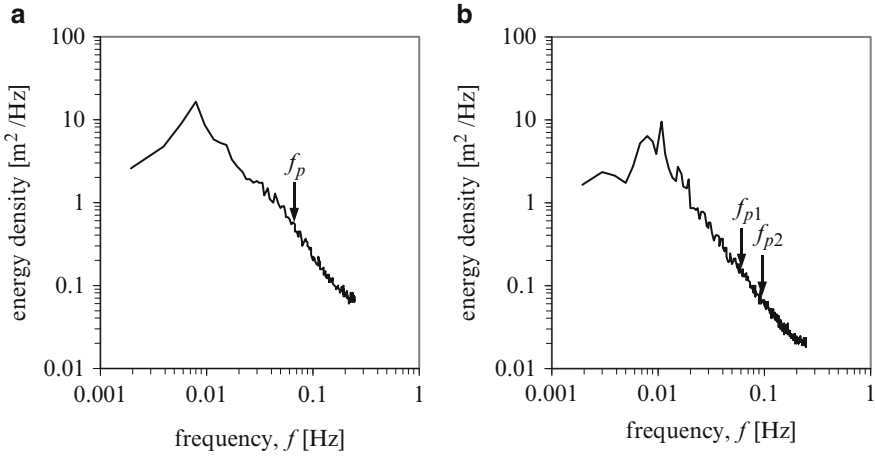


**Fig. 7.19** Longshore-averaged energy density spectra of the water front elevation  $R_f$  for the period of (a) typhoon BANYAN (2005/Jul/26/22 h) and (b) typhoon SAOLA (2005/Sept/25/14 h). Vertical arrows indicate the dominating frequencies of the incident wave fields (discussed in Sect. 7.2.4)

### 7.5.4 Dependence of Run-Up Height on Slope

Surf similarity parameter  $\xi_0$ , a non-dimensional parameter, which is frequently used for examining beach condition and is defined as

$$\xi_0 = \tan \beta / (H_s / L_0)^{1/2} \quad (7.1)$$

where,  $\beta$  is the beach slope,  $H_s$  is the wave height,  $L_0$  is the deep water wave length define as  $L_0 = gT_s^2/2\pi$  by linear theory,  $g$  is the acceleration due to gravity and  $T_s$  is the wave period. Low surf similarity parameters ( $\xi_0 \leq 0.3$ ) typically indicate dissipative condition while higher values suggest more reflective condition.

Surf similarity parameter  $\xi_0$  was estimated using Eq. 7.1 at each cross-shore transect considering sea state conditions for the particular periods as shown in Table 7.2. Foreshore slope at each transect  $\tan \beta$  was also used for the estimates.  $\xi_0$  varied from 0.07 to 0.28 for the period of typhoon BANYAN (2005/Jul/26/22 h) and 0.02 to 0.18 for the period of typhoon SAOLA (2005/Sept/25/14 h) indicating beach conditions were dissipative. Lower surf similarity parameters were observed for typhoon SAOLA period (2005/Sept/25/14 h) compared to that of typhoon BANYAN period (2005/Jul/26/22 h), probably due to milder foreshore slope.

Correlation between the infra-gravity run-up  $R_{ig}$  normalized by significant wave height  $H_s$  and surf similarity parameter  $\xi_0$ ,  $R_{ig}/H_s = a\xi_0 + b$  where  $a$  and  $b$  are regression coefficients, was assessed and is depicted in Fig. 7.20 for both the analyzing periods. Obtained slopes of the best fit lines (i.e., 1.068 during 2005/Jul/25/22 h and 1.265 during 2005/Sept/25/14 h) are in the same order. Several

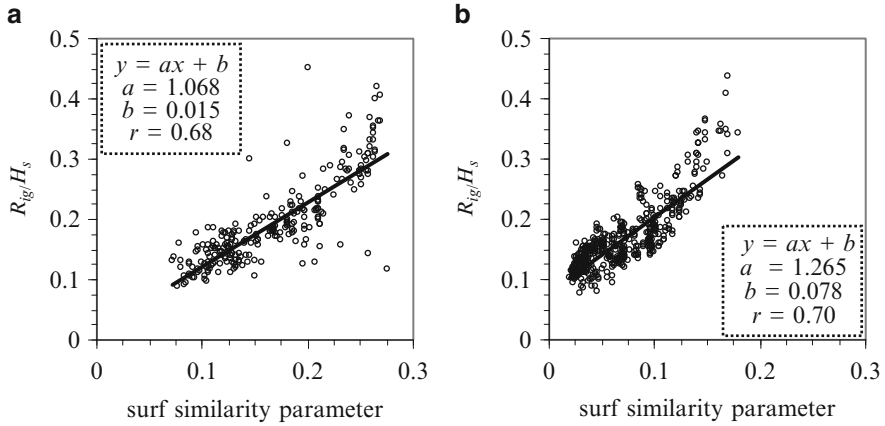


**Fig. 7.20** Infra-gravity band run-up  $R_{ig}$  normalized by the significant wave height  $H_s$  versus surf similarity parameter  $\xi_0$  for the period of (a) typhoon BANYAN (2005/Jul/26/22 h) and (b) typhoon SAOLA (2005/Sept/25/14 h). Best fit lines are  $R_{ig}/H_s = 1.068 \xi_0 + 0.015$  and  $R_{ig}/H_s = 1.265 \xi_0 + 0.078$  (solid lines)

studies (e.g., Holman and Sallenger 1985; Raubenheimer and Guza 1996; Ruessink et al. 1998; Ruggiero et al. 2001; Hasan and Takewaka 2009 etc.) have confirmed this linear dependence between  $R_{ig}/H_s$  and  $\xi_0$ , however, the constant of proportionality is dependent on specific site and sea condition. The linear relationship obtained at Hasaki beach during the energetic sea state is reasonable compared to results obtained at other sites and under different sea conditions.

### 7.5.5 Propagation of Low Frequency Motion

Propagations of large-scale swash-up and -down in the longshore direction were observed visually in the sequence of radar images. A two-dimensional diagram, with the vertical axis for time, and the lateral for longshore extent, was processed to visualize this over the area as shown in Fig. 7.21. The digitized swash front  $S$  of all transects were first converted to elevation  $R_f$  and then separated into infra-gravity band elevation  $R_{f-ig}$  as described above. The time varying  $R_{f-ig}$  was stacked line by line in the diagram to visualize this low frequency motion. Brighter intensities in this diagram correspond to higher run-up values. Inclined streaks are indicating the propagation direction of the low frequency run-up motion. The streaks are clear and inclined for the period of typhoon BANYAN (2005/Jul/26/22 h) as shown in Fig. 7.21a, indicating the run-up variation was propagating in the negative longshore direction. On the contrary, pattern of the streaks are complex for the period of typhoon SAOLA (2005/Sept/25/14 h) as shown in Fig. 7.21b. The figure is suggesting propagations into both negative longshore as well as

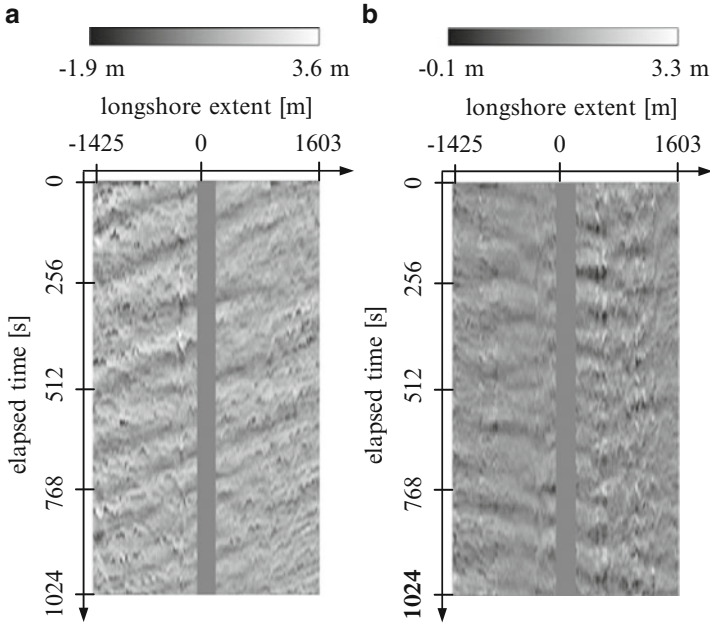


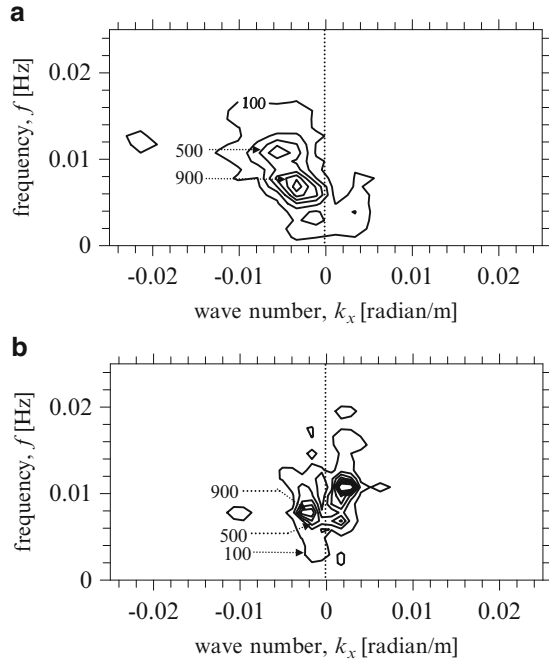
**Fig. 7.21** Longshore propagation of infra-gravity band run-up height variation  $R_{f-ig}$  displayed as image view for the period of (a) typhoon BANYAN (2005/Jul/26/22 h) and (b) typhoon SAOLA (2005/Sept/25/14 h). *Vertical gray stripe* in the middle of the images indicates saturated part in front of the pier which was unable to digitize

positive longshore directions. From these results, we may conclude that the behavior of the low frequency motion is dependent on the incident wave field.

Wavenumber-frequency spectra in the time and longshore domain were estimated for the water front elevations  $R_f$  with the two-dimensional fast Fourier transform (2D-FFT) to investigate the spectral characteristics of the run-up motion over the area. The 2D-FFT was applied to data over a spatio-temporal extent of  $2778.0 \text{ m} \times 1024.0 \text{ s}$  (256 transects  $\times$  512 images, referred to as a sub-area) for the period of typhoon BANYAN (2005/Jul/26/22 h). The estimation was done by shifting the longshore position of the sub-area by 24 times with an interval of 10.85 m (two grid spacing), and then the spectra were spatially averaged in the longshore direction. The size of the sub-area for the period of typhoon SAOLA (2005/Sept/25/14 h) was  $2778.0 \text{ m} \times 1024.0 \text{ s}$  (512 transects  $\times$  512 images) with shifting interval was 5.42 m (one grid spacing). The spatially averaged spectra during both the analyzing periods are shown in Fig. 7.22. Each sub-area includes deficient data due to signal saturation close to the pier, which is shown as the vertical gray stripe in Fig. 7.21. This may interfere with the spectral estimation; however, the result shown in Fig. 7.22 is smooth and has a dominant energy concentration, and it seems that the stripe does not make any severe mischief.

The majority of the energy was concentrated at low wave numbers. The spectrum for the period of typhoon BANYAN (2005/Jul/26/22 h) is clear with distinct

**Fig. 7.22** Wavenumber-frequency spectra of run-up variation  $R_f$  for the period of (a) typhoon BANYAN (2005/Jul/26/22 h) and (b) typhoon SAOLA (2005/Sept/25/14 h). Unit of the spectral intensities is in  $\text{m}^2/\text{Hz}/\text{rad}/\text{m}$



spectral peak in the negative wave number, whereas energy concentrations in both negative and positive wave numbers are observed in the spectrum for the other period (2005/Sept/25/14 h). From the spectrum, estimated peak period and peak wave length was 128.0 s and 1389.0 m during 2005/Jul/26/22 h, whereas the values were 93.1 s and 1389.0 m during 2005/Sept/25/14 h. The order of propagation speed of the low frequency motion in the longshore direction was  $O$  (15 m/s).

Spectral peak obtained at negative wave number for the period of typhoon BANYAN (2005/Jul/26/22 h) corresponds to the propagation of the low frequency run-up motion in the negative longshore direction. Whereas bidirectional propagation (both in the negative and positive longshore direction) was observed for the period of typhoon SAOLA (2005/Sept/25/14 h).

## 7.6 Concluding Remarks

X-band nautical radar measurements were conducted during several storm events in 2005 at the research pier HORS located in Hasaki, Japan. Analyses on echo images were done to estimate the longshore distribution of the mean shoreline positions and inter-tidal foreshore profiles, temporal and spatial variations of the wave run-up and their bulk statistics. Swash fronts were digitized manually from the sequence of radar images and converted to elevations with the help of the foreshore profile.

Low frequency run-up motions during two different stormy wave fields were analyzed and compared in this chapter.

The run-up data were filtered to determine the role of the infra-gravity band component since this band contained most of the total run-up variances, which was observed from their spectral characteristics. The infra-gravity band run-up along an almost 3.0 km length dissipative stretch of coast demonstrates strong dependence on the foreshore slope for both the typhoon periods. Low frequency run-up motion in the longshore direction was observed from the run-up variation. Analyses of the incident wave field revealed single dominant wave incidences for the period of typhoon BANYAN (2005/Jul/26/22 h) and multiple wave incidences for the period of typhoon SAOLA (2005/Sept/25/14 h). The structure of the low frequency motion was clear with organized propagation in the negative longshore direction for the period of typhoon BANYAN (2005/Jul/26/22 h), whereas, complex structure with bi-directional propagation for the period of typhoon SAOLA (2005/Sept/25/14 h).

## References

- Bell PS (1999) Shallow water bathymetry derived from an analysis of X-band marine radar images of waves. *Coast Eng* 37:513–527
- Borge JCN, Rodriguez GR, Hessner K, Gonzalez PI (2004) Inversion of marine radar images for surface wave analysis. *J Atmos Ocean Technol* 21:1291–1300
- Butt T, Russell P (2000) Hydrodynamics and cross-shore sediment transport in the swash zone of natural beaches: a review. *J Coast Res* 16:255–268
- Elfrink B, Baldock T (2002) Hydrodynamics and sediment transport in the swash zone: a review and perspectives. *Coast Eng* 45:149–167
- Gurgel K-W, Antonischki G, Essen H-H, Schlick T (1999) Wellen Radar (WERA): a new ground-wave HF radar for ocean remote sensing. *Coast Eng* 37:219–234
- Guza RT, Thornton EB (1982) Swash oscillations on a natural beach. *J Geophys Res* 87(C1):483–491
- Guza RT, Thornton EB (1985) Observations of surf beat. *J Geophys Res* 90(C2):3161–3172
- Hasan GMJ, Takewaka S (2007a) Observation of a stormy wave field with X-band radar and its linear aspects. *Coast Eng J* 49(2):149–171
- Hasan GMJ, Takewaka S (2007b) Depth-current inversion from a stormy wave field with X-band radar. In: *Proceedings of the Asian and Pacific Coasts on CD-Rom (APAC 2007)*, China, pp 1808–1821
- Hasan GMJ, Takewaka S (2009) Wave run-up analyses under dissipative condition using X-band radar. *Coast Eng J* 51(2):177–204
- Herbers THC, Elgar S, Guza RT (1995) Infragravity-frequency (0.005–0.05 Hz) motions on the shelf. Part II: free waves. *J Phys Oceanogr* 25:1063–1079
- Holland KT, Holman RA (1999) Wavenumber-frequency structure of infra-gravity swash motions. *J Geophys Res* 104(C6):13479–13488
- Holland KT, Raubenheimer B, Guza RT, Holman RA (1995) Runup kinematics on a natural beach. *J Geophys Res* 100(C3):4985–4993
- Holman RA (1981) Infra-gravity energy in the surf zone. *J Geophys Res* 86(C7):6442–6450
- Holman RA (1986) Extreme value statistics for wave run-up on a natural beach. *Coast Eng* 9:527–544
- Holman RA, Boyen AJ (1984) Longshore structure of infra-gravity wave motions. *J Geophys Res* 89(C4):6446–6452

- Holman RA, Sallenger AH (1985) Setup and swash on a natural beach. *J Geophys Res* 90 (C1):945–953
- Hunt IA (1959) Design of seawalls and breakwaters. *J Waterw Harb Coast Eng Div ASCE* 85:123–152
- Inman DL, Guza RT (1982) The origin of swash cusps on beaches. *Mar Geol* 49:133–148
- Miche R (1951) Le Pouvoir reflechissant des ouvrages maritimes exposes a l'action de la houle. *Ann Ponts Chaussees* 121:285–319
- Mizuguchi M, Seki K (2007) Field observation of waves and topographical change near the shoreline. In: *Proceedings of Asian and Pacific Coasts on CD-Rom (APAC 2007)*, China, pp 30–40
- Oltman-Shay J, Howd PA, Birkemeier WA (1989) Shear instabilities of the mean longshore current 2: field observations. *J Geophys Res* 94:18031–18042
- Osborne PD, Rooker GA (1999) Sand re-suspension events in a high energy infragravity swash zone. *J Coast Res* 15:74–86
- Plant NG, Holman RA (1997) Inter-tidal beach profile estimation using video images. *Mar Geol* 140:1–24
- Raemer HR (1996) *Radar systems principles*. CRC Press, Boca Raton, Florida, 544 pp
- Raubenheimer B, Guza RT (1996) Observations and predictions of run-up. *J Geophys Res* 101 (C11):25575–25587
- Raubenheimer B, Guza RT, Elgar S, Kobayashi N (1995) Swash in a gently sloping beach. *J Geophys Res* 100(C5):8751–8760
- Ruessink BG, Kleinhans MG, van den Beukel PGL (1998) Observations of swash under highly dissipative conditions. *J Geophys Res* 103(C2):3111–3118
- Ruessink BG, Miles JR, Feddersen F, Guza RT, Elgar S (2001) Modeling the alongshore current on barred beaches. *J Geophys Res* 106:22451–22464
- Ruggiero P, Komar PD, Marra JJ, McDougal WG, Beach RA (2001) Wave run-up, extreme water levels and the erosion of properties backing beaches. *J Coast Res* 17:407–419
- Ruggiero P, Holman RA, Beach RA (2004) Wave run-up on a high-energy dissipative beach. *J Geophys Res* 109:C06025
- Sallenger AH (2000) Storm impact scale for barrier islands. *J Coast Res* 16:890–895
- Shen MC, Meyer RE (1963) Climb of a bore on a beach, Part 3: run-up. *J Fluid Mech* 16:113–125
- Stockdon HF, Holman RA (2000) Estimation of wave phase speed and nearshore bathymetry from video imagery. *J Geophys Res* 105(C9):22015–22033
- Takewaka S (2005) Measurements of shoreline positions and intertidal foreshore slopes with X-band marine radar system. *Coast Eng J* 47(2 & 3):91–107
- Takewaka S, Nishimura H (2005) Wave run-up analyses during a storm event with nautical X-band radar. *Proceedings of Asian and Pacific Coasts on CD-Rom (APAC 2005)*, Korea, pp 780–788
- Thornton EB, Kim CS (1993) Longshore current and wave height modulation at tidal frequency inside the surf zone. *J Geophys Res* 98:16509–16519
- Wilson GW, Ozkan-Haller HT, Holman RA (2010) Data assimilation and bathymetric inversion in a two-dimensional horizontal surf zone model. *J Geophys Res* 115:C12057